J. Fluid Mech. (1989), *vol.* 198, *pp.* 79–99
Printed in Great Britain

Evolution of locally unstable shear flow near a wall or a coast

By MELVIN E. STERN
Department of Oceanography, Florida State University, Tallahassee, FL 32 306, USA

(Received 10 June 1987 and in revised form 31 May 1988)

An important phase of turbulence production in the flow past a wall occurs with the intermittent inflexional instability of the streamwise current. But according to a linearized inviscid calculation this instability (Kelvin–Helmholtz) can be reduced or eliminated by the presence of a (slippery) wall. Attention is therefore directed to the temporal evolution of a finite-amplitude patch of inflected fluid, i.e. one that is localized in the downstream direction. The model has piecewise uniform vorticity, and the contour-dynamical method is used. Numerical integrations show that sufficiently wide initial patches will eject slow fluid near the wall until it comes into close contact with the free stream, whereupon the ejection is deflected around a large eddy which is surrounded by a stable shear flow. The parametric regime in which this kind of finite instability occurs is sketched, and the Reynolds stress is computed. The initial condition assumed in this calculation depends on the prior existence and intensification of a local spanwise circulation, and this process is briefly discussed using a separate two-dimensional calculation. This shows that widely separated vorticity isopleths tend to completely merge, implying that such fronts in a real fluid may only be viscously limited. The analogous process of *potential* vorticity frontogenesis may be important in oceanic coastal currents.

1. Introduction

Although fully developed turbulent flows must be regarded as stable in the mean (Reynolds & Tiedermann 1967), the classical theory of laminar instability captures a key process which occurs intermittently in space–time. In the flow of a homogeneous fluid past a wall, for example, patches of inflexionally unstable flow associated with large Reynolds stresses develop as a result of local spanwise circulations (Blackwelder & Kaplan 1976; Landahl 1975). An oceanographic illustration of the development of a local instability is given by Send (1988), who attributes the formation of a single large-scale coastal eddy to an isolated region of barotropic instability. It appears that the ever-present large-amplitude disturbances in fully developed laboratory or geophysical flow evolve into locally unstable patches in which one or more eddies develop, and this process is addressed herein.

The simplest calculation of an inflexional instability occurs in the Kelvin–Helmholtz model, consisting of a uniform vorticity layer surrounded by two semi-infinite irrotational layers. Infinitesimal-amplitude disturbances with wavelengths larger than a critical value amplify with time, ultimately concentrating the vorticity into discrete 'cores' (Pozrikidis & Higdon 1985). Let us note that this drastic modification of the laminar shear layer is the way in which the free shear layer achieves a new equilibrium state.

The nature of the equilibration process is expected to be different when a wall

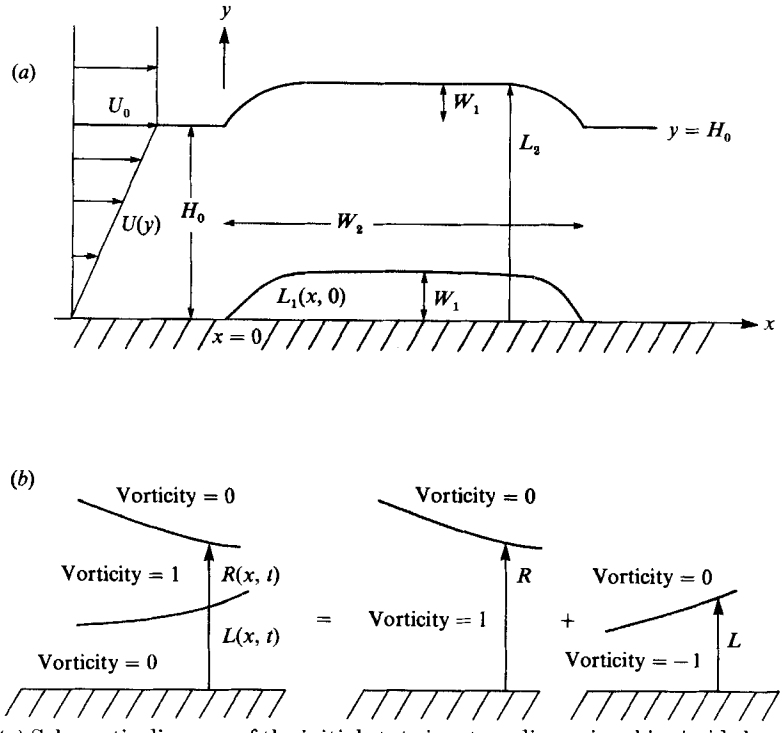

FIGURE 1. (*a*) Schematic diagram of the initial state in a two-dimensional inviscid shear flow whose profile is inflected in the patch of width W_2. Low anticyclonic vorticity and relatively low-velocity fluid lie beneath the lower interface $L_1(x, 0)$, and low-vorticity fluid lies above $L_2(x, 0)$. (*b*) Schematic diagram of the two interfacial heights (R, L) used in the non-dimensional analysis (§2) with the vorticity (cyclonic) of the middle layer being $+1$.

limits the thickness of the lowest layer, because the amplifying wave will remove this fluid before producing drastic changes in the overlying shear layer. The point of departure for our discussion of this effect is the linear stability problem (cf. the Appendix) for a laminar flow with piecewise uniform vorticity. This calculation shows that an inflected shear flow becomes more stable as the ratio of the width of the lower layer to the overlying shear layer decreases.

Our local instability model (figure 1*a*) differs from the preceeding one since it is not a parallel flow. At $t = 0$ we have an irrotational patch of maximum height W_1 and finite width W_2 resting on the wall. This patch perturbs an otherwise stable shear flow, viz. that which exists at $x = \pm\infty$. Thus a vorticity extremum exists over the patch, and the downstream velocity $U^*(x, y, t)$ has an inflected profile in part of this region. How large must (W_1, W_2) be in order that high-momentum fluid be brought into close contact with the wall, and low-momentum fluid in the patch be brought into close contact with the free stream?

2. Formulation of the problem

The equations for a piecewise uniform vorticity flow (figure 1*a*) will be non-dimensionalized using the magnitude of the middle-layer vorticity as the reciprocal time unit, and by using H_0 as the length unit (except where otherwise stated). The ratio of these units gives the velocity unit, and thus the non-dimensional stream function ψ satisfies $\nabla^2\psi = -1$ in the anticyclonic middle layer of figure 1(*a*), or

$\nabla^2\psi = +1$ in the cyclonic middle layer of the schematic diagram figure 1(*b*). It is convenient to use the latter sign for the development in this section, and the sign will be reversed later for the anticyclonic case (figure 1*a*). The non-dimensional velocities are: $v = \mathrm{d}y/\mathrm{d}t = \psi_x$, $u = \mathrm{d}x/\mathrm{d}t = -\psi_y$.

In figure 1(*b*) $R(x,t)$ denotes the non-dimensional height of the upper interface at any t, and $L(x,t)$ is the height of the lower interface. Knowing these heights we can compute (u,v) from Poisson's equation by regarding the left-hand domain in figure 1(*b*) as the sum of the two right-hand domains, having vorticities as indicated. Let ψ_L, ψ_R, denote stream functions associated with each of the domains, i.e.

$$\left.\begin{aligned} \psi &= \psi_R + \psi_L, \\ \nabla^2\psi_R = \begin{cases} 0, & y > R \\ 1, & y < R, \end{cases} \quad \nabla^2\psi_L &= \begin{cases} 0, & y > L \\ -1, & y < L. \end{cases} \end{aligned}\right\} \tag{2.1}$$

The boundary conditions in a coordinate system moving with the fluid at $y = \infty$ are: $\psi_y(x, \infty, t) = 0, \psi_x(x, 0, t) = 0$, and the same boundary conditions are imposed on ψ_R, ψ_L. One may regard the right-hand sides of (2.1) as the sum of elementary vortices of equal strength, each occupying a small area $\mathrm{d}\xi\,\mathrm{d}\eta$, each producing a circularly symmetric logarithmic stream function, and each associated with an image (to satisfy the boundary condition). Summing these elementary responses gives the Green function solutions:

$$\psi_R(x,y,t) = \frac{1}{4\pi}\int \mathrm{d}\xi \int_0^{R(\xi,t)} \mathrm{d}\eta \ln\frac{(x-\xi)^2+(y-\eta)^2}{(x-\xi)^2+(y+\eta)^2}, \tag{2.2a}$$

$$\psi_L = \frac{(-1)}{4\pi}\int \mathrm{d}\xi \int_0^{L(\xi,t)} \mathrm{d}\eta \ln\frac{(x-\xi)^2+(y-\eta)^2}{(x-\xi)^2+(y+\eta)^2}, \tag{2.2b}$$

where the ξ-integration extends over all values of x for which either $R(x,t)$ or $L(x,t)$ are non-zero. On differentiating these to obtain the velocities, we get

$$\frac{-\partial\psi_R}{\partial y} = \frac{1}{4\pi}\int \mathrm{d}\xi \ln\frac{[(x-\xi)^2+[y-R(\xi,t)]^2]\,[(x-\xi)^2+[y+R(\xi,t)]^2]}{[(x-\xi)^2+y^2]^2} \tag{2.3}$$

and a similar expression is obtained for $+\partial\psi_L/\partial y$, with $L(\xi,t)$ replacing $R(\xi,t)$ in (2.3). These two expressions are subtracted to obtain $u(x,y,t)$, the result is evaluated at $y = R(x,t)$ and $y = L(x,t)$, and thus we obtain the Lagrangian contour velocities $\mathrm{d}x_R/\mathrm{d}t, \mathrm{d}x_L/\mathrm{d}t$:

$$\begin{aligned} \frac{4\pi\,\mathrm{d}x_R}{\mathrm{d}t} &= 4\pi\,u(x, R(x,t), t) \\ &= \int \mathrm{d}\xi \ln\frac{[(x_R-\xi)^2+[R(x_R,t)-R(\xi,t)]^2]\,[(x_R-\xi)^2+[R(x_R,t)+R(\xi,t)]^2]}{[(x_R-\xi)^2+R^2(x_R,t)]^2} \\ &\quad - \int \mathrm{d}\xi \ln\frac{[(x_R-\xi)^2+[R(x_R,t)-L(\xi,t)]^2]\,[(x_R-\xi)^2+[R(x_R,t)+L(\xi,t)]^2]}{[(x_R-\xi)^2+R^2(x_R,t)]^2}, \end{aligned} \tag{2.4a}$$

$$\begin{aligned} \frac{4\pi\,\mathrm{d}x_L}{\mathrm{d}t} &= 4\pi\,u(x, L(x,t), t) \\ &= \int \mathrm{d}\xi \ln\frac{[(x_L-\xi)^2+[L(x_L,t)-R(\xi,t)]^2]\,[(x_L-\xi)^2+[L(x_L,t)+R(\xi,t)]^2]}{[(x_L-\xi)^2+L^2(x_L,t)]^2} \\ &\quad - \int \mathrm{d}\xi \ln\frac{[(x_L-\xi)^2+[L(x_L,t)-L(\xi,t)]^2]\,[(x_L-\xi)^2+[L(x_L,t)+L(\xi,t)]^2]}{[(x_L-\xi)^2+L^2(x_L,t)]^2}. \end{aligned} \tag{2.4b}$$

For the v-component of velocity we get (Stern & Pratt 1985)

$$\frac{\partial \psi_R}{\partial x} = \frac{1}{4\pi}\int \mathrm{d}\xi \, \frac{\partial R(\xi,t)}{\partial \xi} \ln \frac{(x-\xi)^2+[y-R(\xi,t)]^2}{(x-\xi)^2+[y+R(\xi,t)]^2} \tag{2.5}$$

and a similar expression for $\partial\psi_L/\partial x$ with $L(\xi,t)$ replacing $R(\xi,t)$. Subtracting these expressions gives the total velocities:

$$\frac{4\pi\,\mathrm{d}R}{\mathrm{d}t} = 4\pi\, v[x,R(x,t),t] = \int \mathrm{d}\xi \frac{\partial R}{\partial \xi} \ln \frac{(x_R-\xi)^2+[R(x_R)-R(\xi)]^2}{(x_R-\xi)^2+[R(x_R)+R(\xi)]^2} - \int \mathrm{d}\xi \frac{\partial L}{\partial \xi} \ln \frac{(x_R-\xi)^2+[R(x_R)-R(\xi)]^2}{(x_R-\xi)^2+[R(x_R)+L(\xi)]^2}, \tag{2.6a}$$

$$\frac{4\pi\,\mathrm{d}L}{\mathrm{d}t} = 4\pi\, v[x,L(x,t),t] = \int \mathrm{d}\xi \frac{\partial R}{\partial \xi} \ln \frac{(x_L-\xi)^2+[L(x_L)-R(\xi)]^2}{(x_L-\xi)^2+[L(x_L)+R(\xi)]^2} - \int \mathrm{d}\xi \frac{\partial L}{\partial \xi} \ln \frac{(x_L-\xi)^2+[L(x_L)-L(\xi)]^2}{(x_L-\xi)^2+[L(x_L)+L(\xi)]^2}. \tag{2.6b}$$

These four Lagrangian integro–differential equations (2.4a, b), (2.6a, b) are valid even if (R, L) are multivalued functions of x, in which case the integrals are contour integrals taken along the respective interfaces, and with $\partial R/\partial\xi\,\mathrm{d}\xi = \mathrm{d}R, \partial L/\partial\xi\,\mathrm{d}\xi = \mathrm{d}L$. In figure 1($a$) there is a 'nose point' and a 'rear point' at which $L_1 = 0$. In the notation of figure 1(b), this becomes

$$\left.\begin{aligned} L(x_{\mathrm{nose}}(t),t) &= 0,\\ L(x_{\mathrm{rear}}(t),t) &= 0,\end{aligned}\right\} \tag{2.7}$$

and the integrals along the lower contour are to be taken between x_{nose} and x_{rear} (whereas the integrals along the upper contour extend from $-\infty$ to $+\infty$). From (2.4b) the velocity of the nose point is

$$\frac{\mathrm{d}x_{\mathrm{nose}}}{\mathrm{d}t} = U_{\mathrm{nose}} = \frac{1}{2\pi}\int \mathrm{d}\xi \ln \frac{(x_{\mathrm{nose}}-\xi)^2+R^2(\xi,t)}{(x_{\mathrm{nose}}-\xi)^2} - \frac{1}{2\pi}\int \mathrm{d}\xi \ln \frac{(x_{\mathrm{nose}}-\xi)^2+L^2(\xi,t)}{(x_{\mathrm{nose}}-\xi)^2}. \tag{2.8}$$

Let us take note of the asymptotic limit $W_1 \to 0$. To obtain the leading term in (2.6a), we set $L = 0, R = 1$ where these terms appear undifferentiated, and this results in a linear equation for $4\pi\,\mathrm{d}R/\mathrm{d}t = 4\pi\,\partial R/\partial t$ (since $u = \mathrm{d}x_R/\mathrm{d}t$ is equal to zero to first order). This shows that the upper interfacial disturbance disperses like an infinitesimal perturbation on the stable shear flow at $x = -\infty$. Therefore, at a fixed $x = O(1), R(x,t)-1$ will ultimately decrease to zero. In order to obtain $L(x,t)$ when $W_1/H_0 \to 0$, we rescale so that $W_1 = \max(L_1(x,0))$ (figure 1a) is the new length unit. Then the velocities on L induced by the R-disturbance are exponentially small $[O(\mathrm{e}^{-H_0/W_1})]$ and negligible compared with the self-interaction velocities associated with L. This means that the lower interface, now at $O(1)$ distance from the wall, 'sees' an upstream flow having uniform shear from $y = 0$ to $y = \infty$. The resulting nonlinear calculation (see §3) for the lower interface will exhibit changes on a long timescale $O[W_2/U(W_1)] \to \infty$ compared with the dispersion time of the upper-level disturbance.

Another interesting limit of (2.4)–(2.6) occurs when the finite variations in $R > 0$ and $L > 0$ occur slowly with x, in which case we set $R(\xi,t) \approx R(x,t)$ and $L(\xi,t) \approx$

$L(x,t)$. Using the fact that the definite integral of $\ln(Z^2+a^2/Z^2+b^2)$ from $Z=-\infty$ to $Z=+\infty$ equals $2\pi(|a|-|b|)$ we get

$$\frac{\partial M}{\partial t}+M\frac{\partial M}{\partial x}=0, \quad \frac{\partial L}{\partial t}+M\frac{\partial L}{\partial x}=-L\frac{\partial M}{\partial x}, \quad M=R-L. \tag{2.9a–c}$$

These long wave equations can be obtained by an elementary calculation using the mass continuity and $\partial u^2/\partial y^2=0$, piecewise.

The hyperbolic equation (2.9*a*) implies that the local separation between the interfaces remains constant relative to an observer moving with a constant speed $M(x,0)$. Therefore, if $M(x,0)$ decreases with x (in some region), then our observer will see $\partial M/\partial x$ approach $-\infty$ as a 'shock' tends to form. Equation (2.9*b*) then implies that the value of L at the shock will increase towards $+\infty$. Since the long-wave solutions of (2.9) are readily obtained and almost always give rise to much smaller scales, we may turn immediately to initial states whose downstream scale is not large compared with the thickness of the shear layer. Furthermore, attention is directed to the most interesting case in which $\partial M(x,0)/\partial x=0$ (since the long-wave theory implies 'nothing', will happen then). This is the reason for choosing a uniform initial thickness (H_0) for the finite vorticity layer in figure 1(*a*).

A verification and understanding of the numerical calculations to be presented in the following sections will be facilitated by the following analytical results.

2.1. *The initial velocities produced by interfaces having the form of step functions*

$$L(x)=\begin{cases}L_-, & x<0\\ L_+, & x>0\end{cases}, \quad R(x)=\begin{cases}R_-, & x<0\\ 1+L_+, & x>0\end{cases} \tag{2.10}$$

(vorticity is positive as in figure 1*b*). For this calculation the thickness of the shear layer on the downstream side of the step provides the length unit. The integrals for v,u at $x=0$ may easily be computed for (2.10), and the results are

$$\begin{aligned}2\pi v(0,y)=&(1+L_+-y)\ln|1+L_+-y|-(R_--y)\ln|R_--y|-(1+L_++y)\ln(1+L_++y)\\&+(R_-+y)\ln(R_-+y)-(L_+-y)\ln|L_+-y|+(L_--y)\ln|L_--y|\\&+(L_++y)\ln(L_++y)-(L_-+y)\ln(L_-+y),\end{aligned} \tag{2.11a}$$

$$4u(0,y)=|y-R_-|-|y-L_-|+R_--L_-+1+|y-1-L_+|-|y-L_+|. \tag{2.11b}$$

From this we see that the nose velocity is

$$u(0,L_-)=\tfrac{1}{2}(1+R_--L_-), \tag{2.12a}$$

and if $R_->L_+>L_-$, then the velocity at the top of this step is

$$u(0,L_+)=\tfrac{1}{2}(1+R_--L_+)<u(0,L_-). \tag{2.12b}$$

Equations (2.12) imply that the face of the lower step will tend to tilt 'upstream' as time increases, and that $L(x,t)$ tends toward a multivalued function of x. If the vorticity in the shear layer is negative the signs of the velocity must be reversed, in which case the slope of the face of the step decreases as times increase.

2.2. *The vortex anomaly concept*

If the total velocity field (u,v) is formally decomposed into the sum of the upstream velocity $U(y)$ plus a residual (u',v), then the total vorticity ζ equals the sum of the upstream vorticity plus a 'vorticity anomaly' ζ'. In figure 1(*a*) these anomalies

are anticyclonic ($\zeta' < 0$) in the area bounded by the upper interface and the line $y = H_0$. These anomalies should induce upward velocities near $x = 0, y = R$, whereas downward velocities ($v < 0$) should be induced near $x = W_2$. (Although the image vortices tend to produce opposite velocities, they are further away from the upper interface and should not change the qualitative conclusion.) The irrotational fluid underneath the L_1 interface contains cyclonic anomalies, which should produce downward velocities near the nose point and upward velocities near the rear point, thereby increasing $\max(L)$ with time. The total motion of any point is obtained by adding the velocity anomalies (u', v) to the undisturbed shear flow $U(y)$ at the point $y = L_1$.

2.3. *The semi-infinite disturbance*

For figure 1 (*a*) the vorticity of the shear layer is negative, so that we must reverse the signs of the velocities in (2.4*a*, *b*) and (2.6*a*, *b*), and then the vertical velocity on the lower interface becomes

$$-4\pi v[x, L(x)] = \int \mathrm{d}\xi \frac{\partial R}{\partial \xi} \ln \frac{(x-\xi)^2 + [L(x) - R(\xi)]^2}{(x-\xi)^2 + [L(x) + R(\xi)]^2} - \int \mathrm{d}\xi \frac{\partial L}{\partial \xi} \ln \frac{(x-\xi)^2 + [L(x) - L(\xi)]^2}{(x-\xi)^2 + [L(x) + L(\xi)]^2}.$$

The last term may be called the self-interaction velocity, the preceeding term may be called the mutual-interaction velocity. We now consider the values of these when $W_2 = \infty$ (in figure 1 *a*), when $L_1(x, 0)$ increases monotonically from $x = 0$ to $x = b$, and when $L_1(x, 0) = W_1/H_0$ for $x \geqslant b$. If $R(x, 0)$ is constant for all x, then the mutual-interaction integral vanishes, and the self-interaction term gives $v[x, L(x, 0)] \leqslant 0$ at all x. Now consider what happens when (as in figure 1 *a*) $R(x, 0) = 1 + L(x, 0)$, and let H denote the non-dimensional value of W_1. Then

$$\begin{aligned} -4\pi \lim_{x\to\infty} v(x, L) &= \lim_{x\to\infty} \int_0^b \mathrm{d}\xi \frac{\partial L}{\partial \xi} \ln \frac{(x-\xi)^2 + [1 + L(\xi) - H]^2}{(x-\xi)^2 + [1 + L(\xi) + H]^2} \\ &\quad - \int_0^b \mathrm{d}\xi \frac{\partial L}{\partial \xi} \ln \frac{(x-\xi)^2 + [H - L(\xi)]^2}{(x-\xi)^2 + [H + L(\xi)]^2} \\ &= \lim_{x\to\infty} \int_0^b \mathrm{d}\xi \frac{\partial L}{\partial \xi} \left[\frac{-4H[1 + L(\xi)]}{G_1} + \frac{4HL(\xi)}{G_2} + O(G_1^{-2}) + O(G_2^{-2}) \right], \end{aligned}$$

where

$$G_1 = (x-\xi)^2 + [1 + L(\xi)]^2 + H^2 = O(x^2), \quad G_2 = (x-\xi)^2 + L^2(\xi) + H^2 = O(x^2).$$

It follows that

$$\lim_{x\to\infty} v(x, L) = \frac{H}{\pi x^2} \int_0^b \mathrm{d}\xi \frac{\partial L}{\partial \xi} = \frac{H^2}{\pi x^2} + O(x^{-3}) \tag{2.13}$$

and these positive velocities at $x \gg b$ are due to the mutual-interaction term, since the self-interaction term is negative. The mutual-interaction term should therefore induce a ridge [$\max(L)(x, t) > H$] at finite x.

2.4. *The momentum transport for an isolated disturbance*

It is well known (and easily shown) that the horizontally averaged vorticity transport $\overline{v\zeta}$ for any continuous velocity field equals $-\partial \overline{uv}/\partial y$, where $\overline{uv}$ is the upward transport of momentum. For the case of figure 1 (*a*) where the vorticity is negative, the total integrated momentum transport is then

$$\mathrm{IMT} = \int_0^\infty \mathrm{d}y \int_{-\infty}^{+\infty} \mathrm{d}x\, uv = \int_0^\infty \mathrm{d}y \int_{-\infty}^{+\infty} \mathrm{d}y (yv\zeta) = (-1) \iint_{S(t)} yv\, \mathrm{d}x\, \mathrm{d}y, \tag{2.14}$$

where the domain S corresponds to the entire shear layer having vorticity $=-1$. S is bounded above by R, bounded below by L, and may be bounded on the sides ($x = \pm\infty$) by oblique straight lines that move with the laminar shear flow in those regions. It then follows that the Lagrangian time derivative in $v = \mathrm{d}y/\mathrm{d}t$ may be commuted with the integrals to obtain

$$\mathrm{IMT} = \frac{-1}{2}\frac{\mathrm{d}}{\mathrm{d}t}\iint_{S(t)} y^2\,\mathrm{d}x\,\mathrm{d}y$$

$$\mathrm{IMT} = \frac{-1}{2}\frac{\mathrm{d}}{\mathrm{d}t}\left[\iint_{D(t)} y^2\,\mathrm{d}x\,\mathrm{d}y - \iint_{Q(t)} y^2\,\mathrm{d}x\,\mathrm{d}y\right],$$

where $Q(t)$ is the fluid area bounded above by $L(x,t)$, and $D(t)$ is the sum of the areas $S(t)$ and $Q(t)$. Thus we have

$$-6(\mathrm{IMT}) = -\frac{\mathrm{d}}{\mathrm{d}t}\left[\int [R^3(x,t)-1]\,\mathrm{d}x - \int L^3(x,t)\,\mathrm{d}x\right], \tag{2.15}$$

where the (-1) has been added to the integrand to make the first contour integral convergent.

If there is no interface above L_1 (i.e. $H_0 = \infty$ in figure 1*a*) then $\zeta' = 0$ outside $Q(t)$. Since $\overline{v(x,y,t)} = 0$, $v(x,\infty,t) = 0$ we have $\overline{v\zeta} = 0$, and $\overline{v\zeta'} = 0$. It follows that the integral of v inside $Q(t)$ vanishes. Therefore the integrated y in $Q(t)$ or the integrated $L_1^2(x,t)$ is an invariant, as well as the integrated L_1.

3. Numerical calculations

Equations (2.4), (2.6) were solved numerically by introducing N_1 Lagrangian points on the lower contour, N_2 on the upper contour, and by using a trapezoidal approximation to evaluate the integrals between successive points. The small interval surrounding the logarithmic singularity was excluded here, and accounted for by means of a separate analytic approximation (see Stern & Pratt (1985) for further details). A separate calculation for the nose point (2.8) and the 'rear point' (figure 1) was also used.

Since the Lagrangian points are only placed in the 'interior' region $x_m < x < x_n$ where v is found to be non-negligible, it is necessary to take account (in (2.4*a*, *b*)) of the contribution to u of the exterior regions (extending to $x = \pm\infty$) where R and/or L are constant. For example, if x_m is the smallest Lagrangian abscissa on the upper interface, then the contribution of the 'left-wing' region $-\infty < \xi < x_m$ to the u-velocity at distant point ($x \gg x_m$) involves terms of the form

$$\int_{-\infty}^{x_m} \mathrm{d}\xi\,\ln\frac{(x-\xi)^2+a^2}{(x-\xi)^2+b^2} = \frac{a^2-b^2}{x-x_m} + O[(x-x_m)^{-2}], \tag{3.1}$$

where (a,b) are independent of ξ and depend on $R(-\infty,t), L(x,t), R(x,t)$. A similar approximation was used to compute the contribution of the 'right wing' (beyond the last point x_n) to the velocity at $x \ll x_n$. The wing corrections (3.1) are not applied to points x too close to the last one (e.g. those with $x_n - x < 3$). These points lie on a horizontal portion of the interface, and consequently they were moved with the undisturbed velocity on the interface. If points near the nose or rear of the lower interface moved upwards, additional points were inserted at each time to maintain adequate spatial resolution, but when the nose moved downwards towards $L = 0$, it

was unnecessary to do this since there was very little fluid below these L-values. When necessary new Lagrangian points were also inserted (or removed) at the ends of the R-interface to maintain resolution. The $4N_1(t) \times N_2(t)$ ordinary differential equations ((2.4), (2.6)) were integrated using a second-order Runge–Kutta approximation with a time step $T = 0.1$ (except for figure 13), and with various suitable choices of the initial point separations $x_i - x_{i-1}$. Over long time intervals, 'surgery' had to be performed, by either removing excessively close interior points or by inserting points to sparse regions, to avoid 'malpractice suits' (especially because an old-fashioned PC was used)! Each 'post-surgery' calculation overlapped the pre-surgery one, thereby providing a check against pathological developments in the operation. These calculations appear to be quite robust, judging by comparison of results with earlier runs using wider point separation.

Preliminary tests of the numerical program were first made using a cyclonic shear layer with the initial conditions

$$\left.\begin{aligned} L(x,0) &= \begin{cases} H_w(1-e^{-x/B}), & x \geqslant 0 \\ 0, & x < 0, \end{cases} \\ R(x,0) &= 1 + H_w, \end{aligned}\right\} \tag{3.2}$$

and with $u(x, \infty) = 0$. One might think of this as a stable coastal current at $x = -\infty$ which decreases linearly to zero as y increases from zero to $1+H_w$, and which converges on a relatively slow downstream current. At $x = +\infty$, this current has velocity $u = 1$ from $y = 0$ to $y = H_w$, and then u decreases linearly to 'zero' at $y = 1 + H_w$. Since the upstream basic flow has cyclonic vorticity, there are anticyclonic anomalies underneath $L(x, t)$ which will induce upward velocities near the nose. This agrees with the quantitative result (2.11*a*) which holds when $B \to 0$. For the latter case a run of our numerical program gave initial velocities with errors of 1 % or less (due mainly to the finite interval of discretization). For small B, (2.12) suggests an initial steepening of the nose of the front. Figure 2 confirms this for $B = 0.5$, $H_w = 0.5$, and shows $L(x, t)$ becoming multivalued after the initial interval $(0 < t < 3)$ of nose steepening. We found that at $t = 0, 3, 9$ the nose velocity (equation (2.8) was 1.41, 1.20, 1.08 respectively. By comparing these values with $u(-\infty, 0, t) = 1.5, u(+\infty, 0, t) = 1.0$, we see that particles near the wall are decelerated as they approach the nose, and then they are deflected backwards in the plume ($t = 9$) produced by the downstream convergence. But the rate of increase of area in the multivalued plume eventually decreases with t because the nose velocity approaches the uniform velocity of the irrotational wall layer at $x = +\infty$. Note that despite the infected velocity profiles at $x > 0$ there is very little displacement at $t = 9$ of the upper interface, and this result is remarkably different from the following calculation.

We now consider the case in which a fast anticyclonic shear layer at $x = -\infty$ converges on a slow current (at $x = +\infty$), such as occurs in figure 1(*a*) when $W_2 = \infty$ and $u(-\infty, 0, t) = 0$ (now the coordinate system moves with the wall velocity at $x = -\infty$). For the initial condition

$$\left.\begin{aligned} L(x,0) &= H_w \begin{cases} 1-e^{-x}, & x \geqslant 0 \\ 0, & x \leqslant 0, \end{cases} \\ R(x,0) &= 1 + L(x,0) \end{aligned}\right\} \tag{3.3}$$

(anticyclonic shear layer) the basic velocity at $x = -\infty$ increases linearly from zero at $y = 0$ to $u = 1$ at $y = 1$, and then remains constant at $y \geqq 1$. At $x = +\infty$, $u = 0$

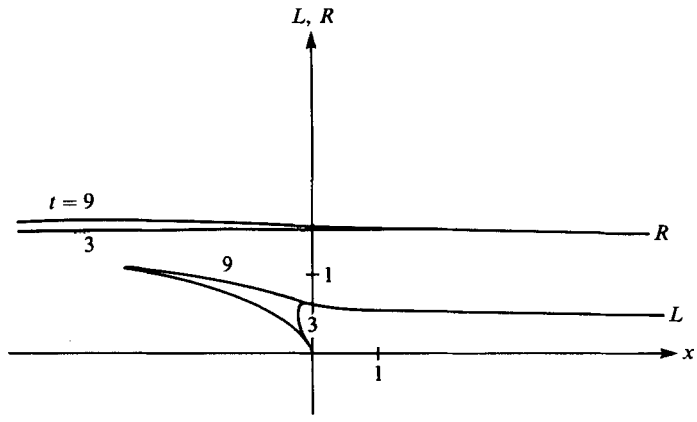

FIGURE 2. The evolution of a 'fast coastal current' (at $x = -\infty$) converging on a relatively slow one (at $x = +\infty$). The upper interface separating the irrotational fluid from the cyclonic shearlayer is initially horizontal. The initial shape of the lower interface separating the shear layer from the irrotational wall layer is given by (3.2). The origin ($x = 0$) of the coordinate system moves with the nose point. At $t = 9$ there are $N_1 = 93$ points on the lower interface and $N_2 = 52$ points on the upper one. The scale for the ordinate (labelled L, R in the figures) is the same for the two interfaces.

from $y = 0$ to $y = H_w$, and then u increases linearly to $u = 1$ at $y = 1 + H_w$. Thus at any y we have relatively slow flow at the downstream end.

The numerical results for $H_w = 0.50$ (figure 3) are displayed in a coordinate system moving with the nose point. At $t = 0$ the velocity of this relative to the velocity at $(x = -\infty, y = 0)$ is -0.13, and the velocity at $(x = 1.95, y = 0.428)$ is -0.5 relative to the velocity at $(x = \infty, y = 0.428)$. (These negative velocities may be rationalized by referring to the calculation (2.12*b*) for a 'step-L', and by using the appropriate sign for ζ.) Figure 3 verifies that the cyclonic anomalies under L are dominant in producing downward displacements at the nose of L, and the ridge formation further downstream is explained by (2.13). Mass is therefore displaced from under the nose region into the lower ridge. The ridge formation on the upper interface at $t = 4$ is explained by the dominance of the anticyclonic anomalies underneath R. In the early stages (figure 3*a*) the relatively rapid downstream propagation of the upper ridge is expected because of the greater mean speed there. Thus the minimum thickness of the finite vorticity layer decreases, and on the basis of the linear theory (see the Appendix) we expect the short-wavelength ridges to amplify along with phase locking (equal phase speeds). This occurs with the upper ridge located further downstream than the lower ridge. Then it is easy to see that the cyclonic anomalies under the L-ridge induce upward motion in the R-ridge, the anticyclonic anomalies under the R-ridge induced upward motion in the trailing L-ridge, and thus we obtain ($t \geqslant 10$) the amplification of both ridges. Of course dispersion also occurs, and this leads to the downstream troughs ($t = 16$). The downward displacement of the R-trough exceeds that of the L-trough because the latter is inhibited by the wall (figures 3*b*, 3*c*). This is a key phase of the process because fluid from the high-velocity region above the inflexion is transferred to the near-wall region. The formation of the large anticyclonic eddy (note the vertical exaggeration) is completed by the slow fluid near the wall being ejected to large y and wound around the perimeter of the eddy core. It also appears (figure 3*c*) that a second eddy will eventually form downstream of the first one. Similar effects are produced on a longer timescale when H_w is reduced by half (figure 4). Although velocity reversals relative to $u(-\infty, 0, t)$ occur in these large

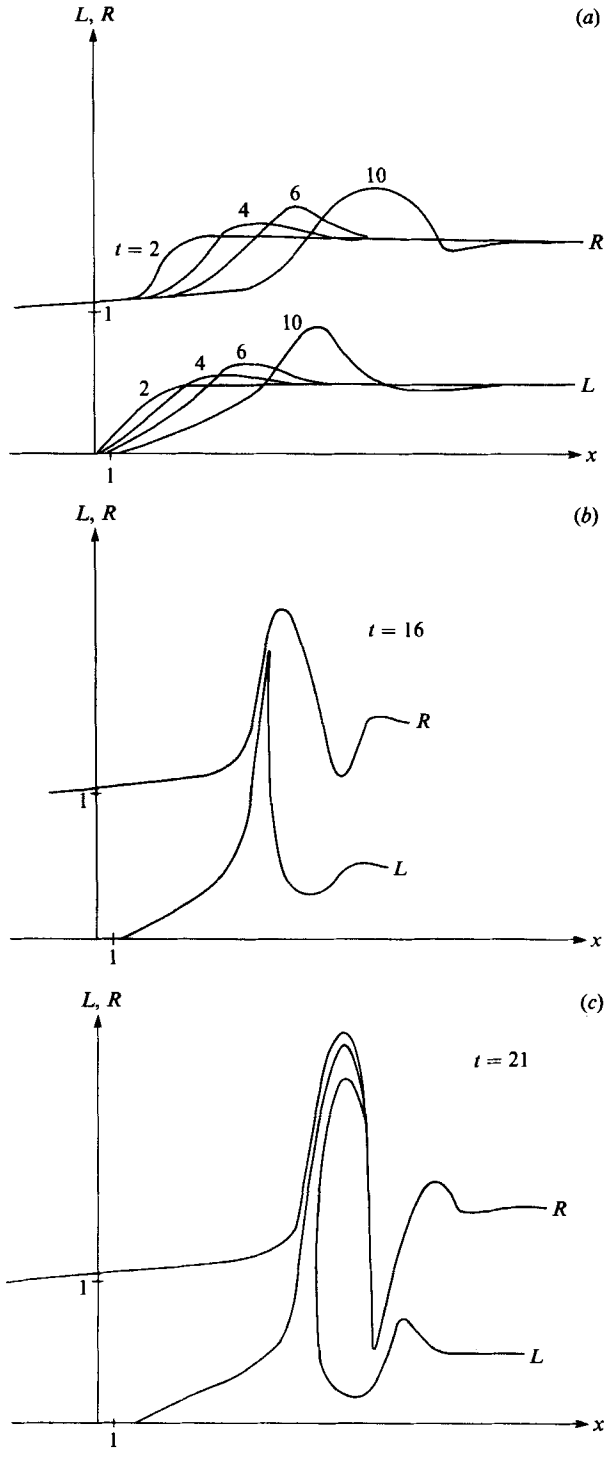

FIGURE 3. The evolution of a local instability from a locally stable region for the initial conditions in (3.3). (*a*) The early stage showing the phase locking and amplification of the ridges on the two interfaces. (*b*) Note the amplifying trough at $t = 16$, at which time $N_1 = 127$ and $N_2 = 173$. (*c*) The later stage in which an anticyclonic eddy forms. (Note the scales and the vertical exaggeration.) At $t = 21, N_1 = 154, N_2 = 198$.

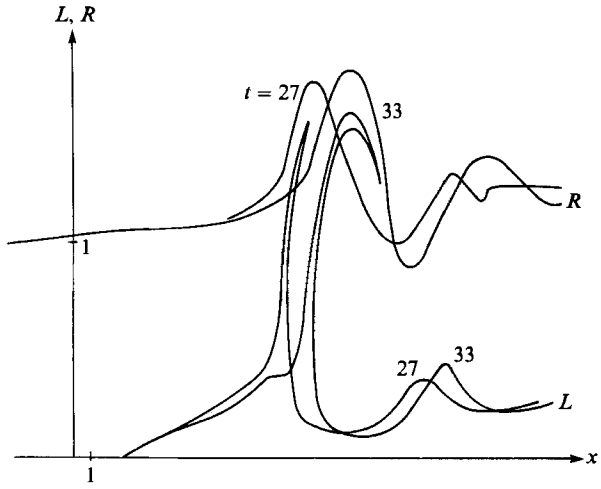

FIGURE 4. Same as figure 3 except $H_w = 0.25$. On the lower interface at $t = 27$, $\min(L)$ is at $x = 16.6$. At $t = 33, N_1 = 226, N_2 = 259$, but the last Lagrangian points have been omitted. Also the points near $x = 0$ do not appear because their ordinate is very small.

eddies, one must remember to associate our $y = 0$ level with some height above the viscously dominated region of a fully turbulent wall flow.

The foregoing calculations correspond to $W_2 = \infty$ in figure 1(*a*), and we now consider the case of finite W_2 as given by the initial condition

$$\left.\begin{aligned} L(x,0) &= H_w \begin{cases} 0, & x < 0 \\ 2 - \cosh a(x/x_n - 1), & 0 < x < 2x_n \\ 0, & x < 2x_n, \end{cases} \\ R(x,0) &= 1 + L(x,0), \\ \cosh a &= 2 \end{aligned}\right\} \tag{3.4}$$

(anticyclonic shear layer).

In this case the upstream ($x = -\infty$) and downstream ($x = \infty$) profiles are identical (and the same as the upstream flow in the previous case). But now there is a compact region of slow (irrotational) fluid between the nose point ($x = 0$) and the rear point ($x = 2x_n$). When $H_w = 0.5$, $x_n = 5$ the evolution (figure 5) is similar to that obtained for (3.3) with $H_w = 0.5$, insofar as a large anticyclonic eddy forms which transports upper-layer fluid to the wall and transports lower-layer fluid to large y. Relative to $x = -\infty, y = 0$, the initial nose velocity is -0.083 and the initial rear-point velocity is -0.084, the small difference being partially due to asymmetry in the distribution of the Lagrangian points and partially due to numerical errors in evaluating the integrals. At $x = 4.95$, the downstream velocity on L is -0.42 relative to the upstream velocity at the same y. The main difference between figure 5(*c*) and figure 3(*c*) is that a sufficiently large portion of the low-speed patch is removed from the wall by the anticyclonic eddy, so that the shear flow will reach a statistically stable state with no additional eddies.

The results shown in figures 6 and 7 are explained by the asymptotic analysis in §2, which indicates that as $H_w \to 0$ with fixed finite x_n the two interfaces decouple, the evolution on the upper one being given by linear theory. With $H_w = 0.1, x_n = 2.5$ (figure 6), the upper interface shows the dispersion of the small-amplitude disturbance, such as occurs in the flow of a completely stable shear layer over a rigid

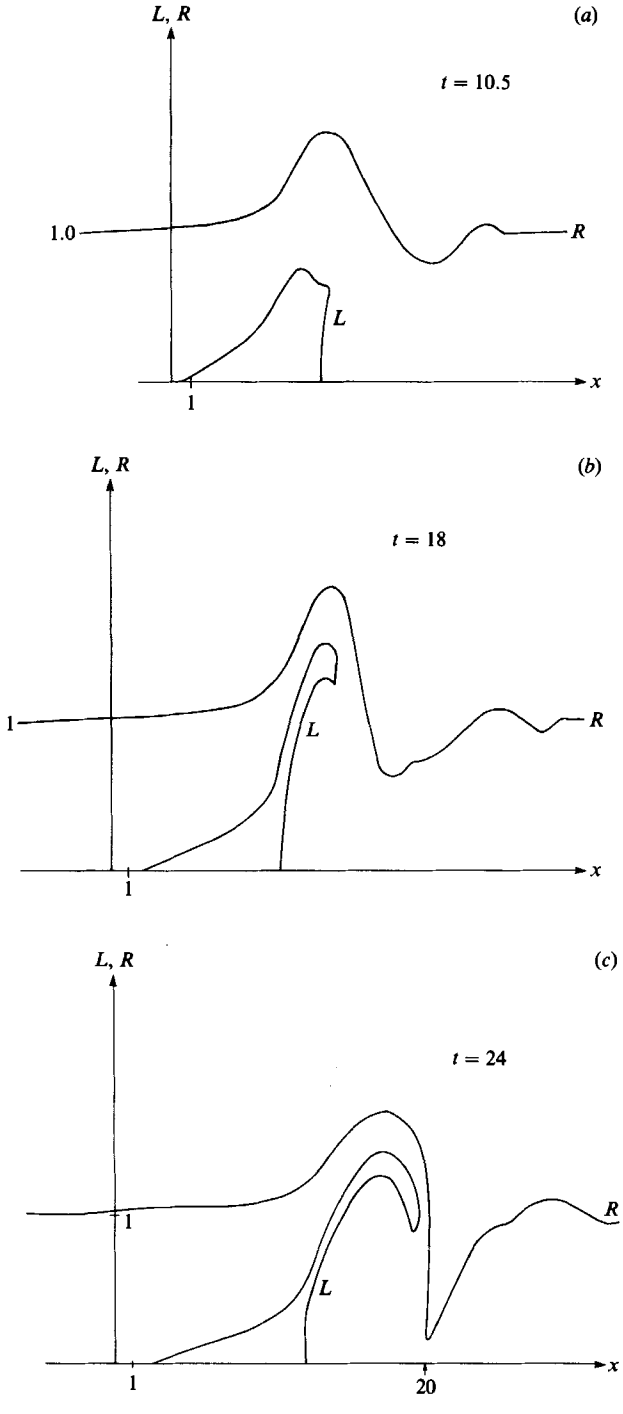

FIGURE 5. The evolution of local instability where there is a compact region of low velocity near the wall. $H_w = 0.5, x_n = 5$. (*a*) $N_1 = 75, N_2 = 196$. (*b*) $N_1 = 86, N_2 = 234$. (*c*) $N_1 = 103, N_2 = 264$. The last Lagrangian point is at $x = 39.5$. The time step is $T = 0.1$.

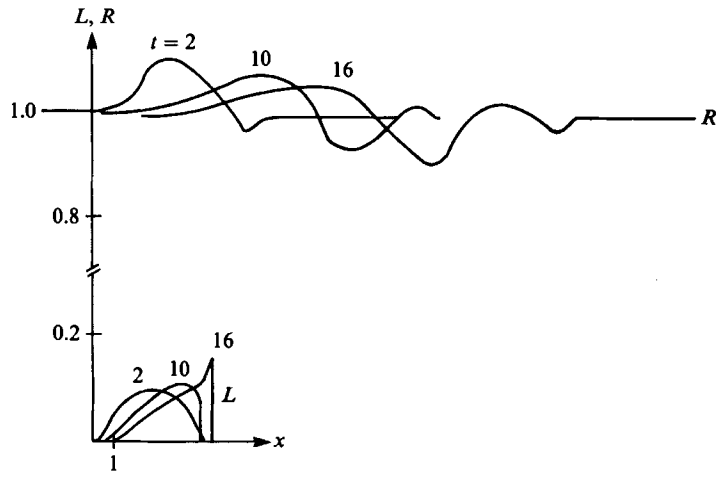

FIGURE 6. The 'stable' evolution which occurs for small $H_w = 0.1$ and $x_n = 2.5$. At $t = 16, N_1 = 57$, $N_2 = 209$. The disturbance on the upper interface evolves in an essentially linear way. The lowr interface is highly nonlinear; e.g. a tip of the low-speed fluid is ejected ($t = 16$) into the shear layer (note the scale break on the ordinate). But this has little effect on the upper interface and no anticyclonic eddy forms.

boundary ($y = 0$). On the lower interface a thin tip of the slow fluid is ejected into the lower layer and carried downstream, without much influence on R.

The behaviour of the lower interface was qualitatively checked by the calculation for figure 7, in which the upper interface is completely removed (from the numerical program) and the upstream flow has constant shear from $y = 0$ to $y = \infty$. For this one interface we rescaled using the maximum value of $L(x, 0)$ as the lengthscale (the inverse vorticity is still the timescale), and using the initial condition

$$L(x,0) = \begin{cases} 0, & x < 0 \\ 2 - \cosh a(x/x_n + 1), & -2x_n < x < 0, \\ 0, & x < -2x_n, \end{cases} \qquad \cosh a = 2 \tag{3.5}$$

(anticyclonic shear extending to $y = \infty$).

In this calculation the origin ($x = 0$) of the coordinate system is fixed (relative to the wall), and we took $u(-\infty, 1) = 0$, so that the wall velocity at $x = \pm\infty$ is negative. Note that the $y = \infty$ boundary condition in this problem is different from the preceding one and, moreover, we only have cyclonic anomalies (underneath L). Since these anomalies (and their images) cause $u(x, 0)$ to increase with $x > 0$, we now have a fast patch of irrotational fluid on the wall, and therefore this initial state is not a complete asymptotic limit to the previous one. But the cyclonic anomalies do produce downward motion at the nose (figure 7) and upward motion at the rear, thereby causing an ejection of the low-vorticity flow. Although this qualitative behaviour of L is similar to figure 6, we now have fast fluid being transported upwards thereby producing a momentum flux up the mean gradient. From $t = 0$ to $t = 10$ the area under L and the area under the L^2 curve remained constant to better than 1%, whereas both these areas are conserved according to the last paragraph in §2.4.

When the initial patch width in figure 5 is reduced to $x_n = 2.5$ with $H_w = 0.5$ held constant, an unstable region and a large anticyclonic eddy also form (figure 8) as in

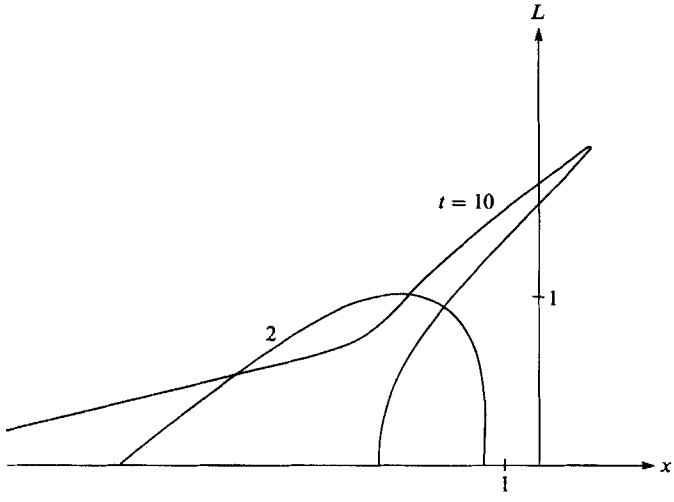

FIGURE 7. This is similar to figure 6 except that the upper interface is removed (to $y = \infty$) and the calculation is rescaled (see text). The origin ($x = 0$) in this calculation is fixed relative to the wall. The important point to note is the ejection of a plume of low vorticity into the overlying anticyclonic shear layer, this effect being similar to that in figure 6.

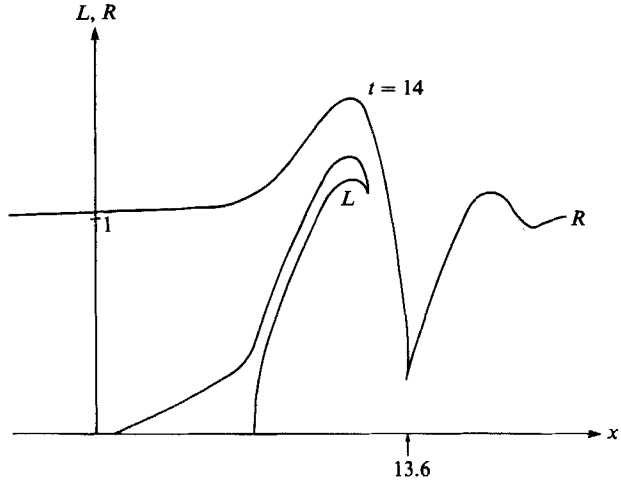

FIGURE 8. Same as figure 5 except $x_n = 2.5, H_w = 0.5, N_1 = 91, N_2 = 219$.

figure 5. The reason why the formation time is slightly shorter in figure 8 is that the initial interfacial slopes (and $|v(x, 0)|$) are larger near the nose and rear points. (Also note that the x- and L-scales are different in figure 5*c* and figure 8.)

A calculation (not shown) was also made for $H_w = 0.25, x_n = 2.5$ and the evolution was similar to figure 6, especially with regard to the dispersive wavetrain which develops on the upper interface. For example, at $t = 14$, the important first trough on R is at $x = 14.3, y = 0.77$ which is far downstream from the rear point (at $x = 6.2$) on the lower interface. These particles originally near the upper interface always remain far from the wall and do not form an anticyclonic eddy. On the other hand the plume [max (L)] on the lower interface extends to a larger $y = 0.68$ than in figure 6, but this plume is so thin that it cannot overcome the dispersion effects on R which lead to a reduction in max R as t increases.

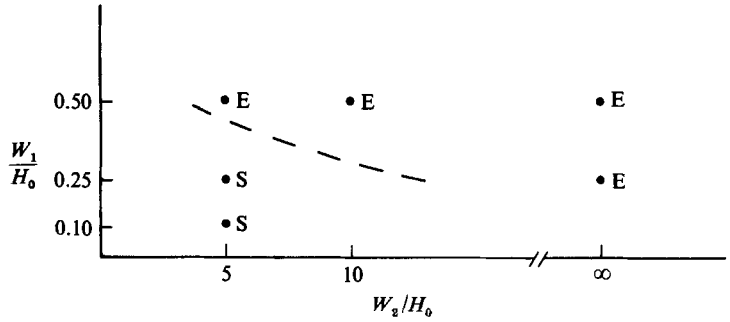

FIGURE 9. Regime diagram for the local instability in figure 1(*a*), E denotes a run in which $\max(L_1) > H_0$, and a large anticyclonic eddy (E) forms. The symbol S on the other hand, indicates that only a dispersive wave forms on the upper interface.

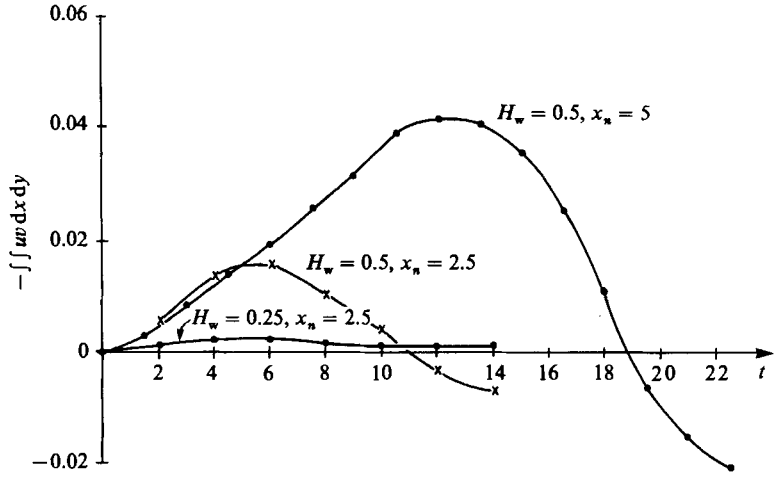

FIGURE 10. The downward momentum transport integrated over all x, y in those cases where the patch is isolated.

4. Discussion

The numerical results are summarized in the regime diagram of figure 9, where W_1, W_2, H_0 are the dimensional parameters in figure 1. The symbol E indicates that the maximum nondimensional height reached by the lower interface is at least as large as $y = 1$, the undisturbed lower boundary of the free stream. In this case at least one large anticyclonic eddy evolves, bringing fluid from above the inflexion into close contact with the wall. The symbol S, on the other hand, indicates an evolution in which $\max(L(x,t)) < 1$, and particles on the upper interface remain in the vicinity of $y = 1$ at all times. No anticyclonic eddy forms, but a thin plume of irrotational fluid is ejected from the downstream side of L into the overlying shear layer where it is strained and eventually entrained.

Figure 10 shows the temporal variation of the non-dimensional average momentum transport (equations (2.14)–(2.15)) for the finite-patch models. Because of the symmetry of the initial interfacial disturbances, the momentum transport is zero at $t = 0$. At subsequent times the mean momentum transport increases to a maximum as the eddy grows, then decreases as the eddy equilibrates and as the source of the inflexional instability is removed. The numerical calculations show that the

maximum momentum transport increases with patch width and amplitude H_w. After the anticyclonic eddy reaches maturity and the upper interfacial disturbance starts to disperse, the momentum transport changes sign.

5. Remarks on the spanwise circulation

In the foregoing work we considered the streamwise effects in a boundary layer, by incorporating the effect of the spanwise circulation as an initial condition. Now we shall reverse the procedure by neglecting the streamwise variations, and calculate the evolution of an initially weak spanwise circulation. The important half of the latter will be modelled by a semi-infinite wall jet (or half-jet) intruding into an irrotational region, viz.

$$R(x,0) = (1+H_w)\begin{cases} 1-e^{-x/B}, & x>0 \\ 0, & x<0, \end{cases} \tag{5.1}$$

$$L(x,0) = H_w \quad \begin{cases} 1-e^{-(x-1)/B}, & x>1 \\ 0, & x<1, \end{cases} \tag{5.2}$$

$$U(x,\infty,t) = 0, \tag{5.3}$$

$$\text{vorticity below } L = \zeta, \tag{5.4}$$

$$\text{vorticity immediately below } R = -1. \tag{5.5}$$

For constant B this gives a semi-infinite wall jet flowing from positive x towards an irrotational fluid lying outside the upper interface.

When $\zeta = -1$, this problem reduces to the one-interface problem considered by Stern & Pratt (1985), who showed that for large B the nose of $R(x,t)$ steepens with time, reaching a quasi-equilibrium state with $O(1)$ slope. The steepening vorticity isopleth amplifies the vertical velocity, and we shall now show that an additional amplification occurs when $\zeta < -1$ because the two interfaces merge (frontogenesis). This effect corresponds to an extreme increase in the x-gradient of vorticity in a continuously varying fluid (Stern & Vorapayev 1984).

The contour-dynamical calculation for this section differs from the previous ones only insofar as there is a nose point on both interfaces. The modified program for this problem was checked by computing the initial velocities for step functions ($B \to 0$) in R, L, and by comparing the result with an analytic calculation (cf. (2.11 *a*, *b*)). For a stable jet with $\zeta = -2$ and with a rather large B, figure 11 shows a strong frontogenetical effect as the nose regions of the two interfaces merge. Figure 12 suggests that the nose curvature eventually becomes independent of its initial shape, in agreement with the one-interface calculation of Stern & Pratt (1985), but figure 13 indicates that the curvature does depend on H_w. The final nose speeds in figures 11, 12, and 13 are -0.67, -0.67, -0.90 respectively.

A similar effect is seen (figure 14) for the case of the half-jet ($\zeta = 0$). At $t = 12$ we again see the remarkable merging of the two interfaces, suggesting that the analogous effect in a real fluid may only be limited by viscosity. In any case the inescapable conclusion is that initially weak vertical velocities at the nose of a spanwise intrusion will amplify, thereby lifting relatively low streamwise velocities above the wall region, setting the stage for the inflexional instabilities discussed previously. (Perhaps a downstream modulation of the latter process would be sufficient to initiate the streamwise circulation discussed in this section, and to couple the two kinds of two-dimensional mechanisms.)

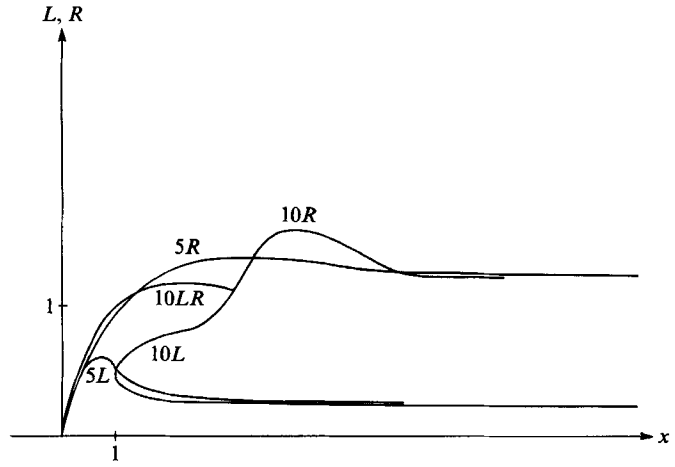

FIGURE 11. Vorticity frontogenesis (see text). The label $10L$ indicates the lower interface at time 10, $10R$ indicates the upper interface at $t = 10$, $10LR$ indicates the merged segments at $t = 10$, and similar conventions are used in all following figures. $H_w = 0.25, B = 1.5, \zeta = -2$. The lower interface converges on the upper interface in a coordinate system moving with the nose point ($x = 0$) of the latter. The velocity profile at $x = +\infty$ consists of a wall jet with irrotational fluid at $y = \infty$ and also at $x = -\infty$. At $t = 10, N_1 = 156, N_2 = 136$. In this, and all the following diagrams, Lagrangian points were inserted and deleted automatically at each time step ($T = 0.1$) to maintain a specified spatial resolution.

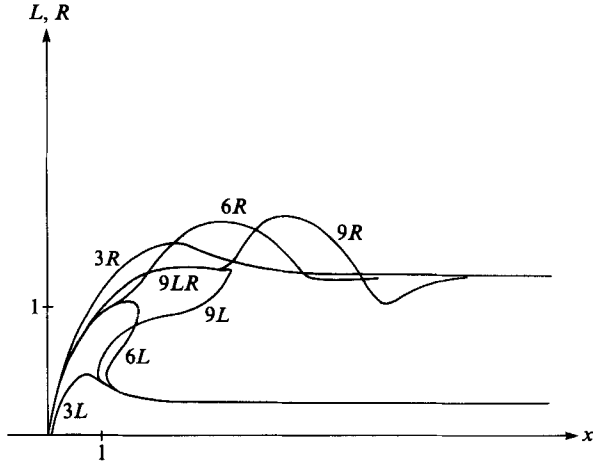

FIGURE 12. Same as figure 11 except at $B = 0.5$. Note the coincidence of the two fronts in the nose region.

The final diagram (figure 15) shows what happens in the different case of a full jet: $\zeta = +4$ (and $H_w = 0.25, B = 1.5$), for which the wall velocity vanishes at $x = +\infty$. At $t \leqq 4$ the two nose points start to merge but the large cyclonic vorticity ($+4$) near $y = 0$ prevents the lower portion of the fluid from making an anticyclonic turn at $x = 0$. Instead we have at $x = 0, t = 16$ a finite separation between the noses of the two interfaces (together with the instability wave at larger x). The implication for the spanwise circulation in a real fluid is that vorticity frontogenesis will occur at some distance above the wall, and in regions where the vorticity gradient is monotonic.

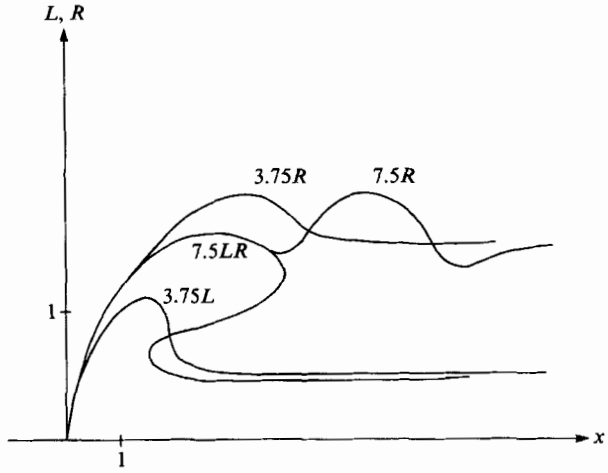

FIGURE 13. Same as figure 12 except a larger $H_w = 0.5$. Extreme frontogenesis in the nose is again indicated. $T = 0.075$ and at $t = 7.5, N_1 = 160, N_2 = 113$.

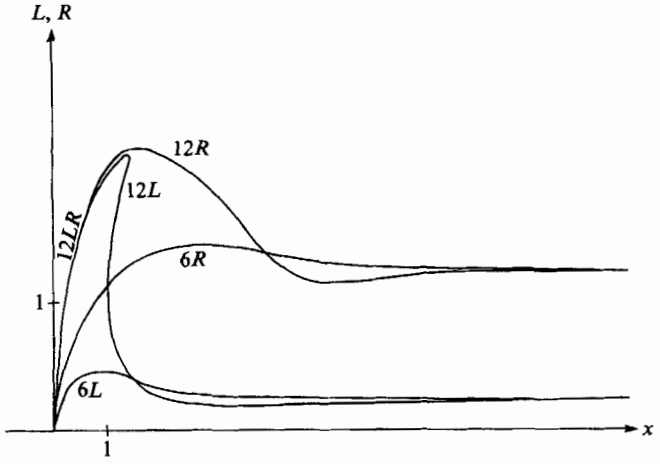

FIGURE 14. Vorticity frontogenesis in the half-jet $\zeta = 0, H_w = 0.25, B = 1.5, T = 0.1$. At $t = 12$, $N_1 = 151$, $N_2 = 148$, and the nose speed is -0.33.

6. Conclusion

Although the presence of a rigid boundary tends to stabilize an inflected laminar shear layer, a strong finite-amplitude instability can develop when the initial state (figure 1*a*) contains an isolated wall patch with relatively low speed and low vorticity. Fluid is squeezed out of the upstream nose as the faster fluid converges on it, and ejected upwards at larger x. As the concomitant upper-level ridge propagates more rapidly downstream there is an increase in 'local instability' as (formally) measured by the ratio of layer thickness. Thus the propagation speeds on the two interfaces equalize and phase lock, with the upper ridge (having anticyclonic vorticity anomaly) downstream from the lower ridge (having cyclonic anomalies). The anomalies in each ridge cause the other ridge to amplify, and downstream troughs are also produced by dispersion. Then the lower-layer ridge approaches the upper interface, the amplifying upper-layer trough approaches the wall, and a large

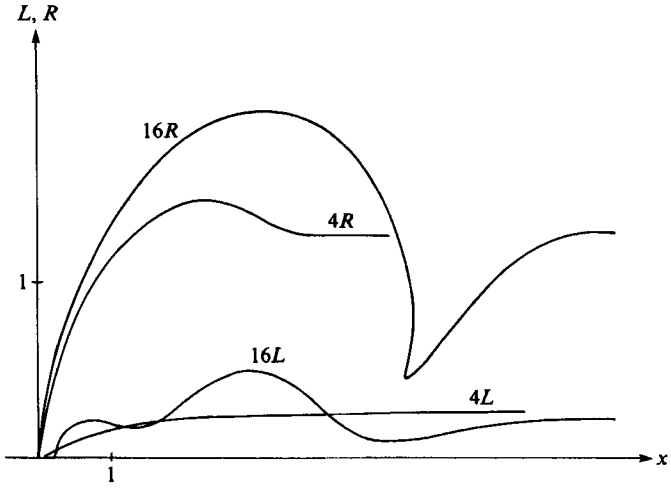

FIGURE 15. A full jet: $\zeta = +4, H_w = 0.25, B = 1.5$. At $t = 16, N_1 = 87, N_2 = 120$. The leading nose velocity is -0.44, and the trailing nose velocity is -0.35. Note the inflexional instability of the jet at $t = 16$. The main point, however, is that the interfaces do not merge in regions where the vorticity changes sign.

anticyclonic eddy forms in the region of the original inflexion. If W_2 (figure 1*a*) is large enough (compared with the vertical thickness of the inflected layer) then additional eddies may form successively in time and further downstream.

The regime diagram (figure 9) indicates the conditions under which the evolution of the lower interface causes it to make close contact with the free stream by attaining a maximum height of $y \geqslant 1$. A more detailed calculation of the finite-amplitude-regime boundary (i.e. the dashed curve) does not seem warranted at this stage because it depends on the detailed shape of $L_1(x, 0)$ as well as (W_1, W_2). Nevertheless the trend of the boundary seems well established, and we expect the curve to level off at some small finite W_1/H_0 below which there is too little fluid available for the lower interface to reach $y = 1$. Unlike the free shear layer, restabilization is achieved by the removal of the fluid below the main shear layer.

For $W_1/H_0 = 0.5, W_2/H_0 = 10$ (figure 1*a*) the temporal maximum of the Reynolds stress (figure 10), divided by the patch area ($0.5 \times 10 = 5$) equals $0.04/5$, where the unit of velocity is the change across the inflected layer. For an order-of-magnitude calculation suppose that this velocity is $\frac{1}{2}$ of the free-stream velocity F in the turbulent flow over a wall, so that the patch average (of the max t) Reynolds stress equals $(0.04/5)(\frac{1}{2}F)^2 = 20 \times 10^{-4}F^2$. According to Hinze (1959, figures 7–14), the space–time-averaged Reynolds stress in the lower boundary layer is half the wall stress or $\sim 5 \times 10^{-4}F^2$. Thus our calculations indicate that much larger values may occur intermittently in connection with inflexional patches. It is hardly necessary to mention that our calculations must be placed in proper perspective, with proper reservations, when applied to turbulent flow over a rigid boundary. The three-dimensional spanwise motions (see §5) which occur there are necessary to establish the inflexional patch assumed in our two-dimensional theory, and very small-scale three-dimensional instabilities are also observed on the back side of the large-amplitude Kelvin–Helmholtz waves (Lasheras, Cho & Maxworthy 1986). The purpose of this paper has been to isolate and explain part of the whole problem.

Our finite-amplitude-instability calculation may be applicable to the oceano-

k	c	ω	$\bar{W}$
1.25	0.508	1.092	1.25
1.15	0.537	1.48	0.714
0.9	0.619	3.10	0.372
0.8	0.654	4.24	0.300
0.7	0.691	5.93	0.243
0.6	0.730	8.57	0.195
0.5	0.771	13.0	0.154
0.4	0.813	21.4	0.116
0.3	0.858	39.7	8.4×10^{-2}
0.2	0.903	93.1	5.4×10^{-2}
0.1	0.951	386	2.6×10^{-2}
0.05	0.975	766	2.6×10^{-2}
0.01	0.995	399.0×10^{2}	2.5×10^{-3}
0.001	0.995	117.0×10^{4}	8.0×10^{-4}

TABLE 1. The neutral wave

graphic problem mentioned in the Introduction, since 'new' large-scale eddies appear only intermittently, and in a setting that does not resemble the highly unstable laminar current which is usually postulated as a starting point. The frontogenetical mechanism discussed in §5 also seems relevant because it appears to be a consequence of the existence of a quasi-two-dimensional invariant (vorticity), and in the ocean this property is attained by the potential vorticity. Since temperature, salinity, and density are also quasi-invariants the formation of fronts in these properties might occur concomitantly.

I would like to acknowledge stimulating discussions on this subject with Mr Uwe Send at the GFD summer school, and financial support by ONR and NSF.

Appendix. Linear instability theory for a horizontally uniform shear flow near a wall

Consider a shear flow of unit (non-dimensional) vorticity located between $y = 0$ and $y = 1$ with a wall at $y = -\bar{W}$, with mean velocity $\bar{U}(y) = 1$ in $0 > y > -\bar{W}$, and with $\bar{U}(y) = 0$ in $\infty > y > 1$. Apply infinitesimal perturbations of wavenumber k, phase speed c, and a stream function equal to the real part of $\hat{\psi}(y)\, e^{ik(x-ct)}$, where

$$\hat{\psi} = \begin{cases} (\cosh k + A \sinh k)\, e^{-k(y-1)}, & \infty > y \geqslant 1 \\ \cosh ky + A \sinh ky, & 1 \geqslant y \geqslant 0 \\ \sinh k(y+\bar{W})/\sinh \bar{W}k, & 0 \geqslant y \geqslant -\bar{W}, \end{cases}$$

and where the integration constant A must be chosen such that the downstream pressure gradient is continuous at $y = 1$ and $y = 0$. This requires continuity of $-(\bar{U}(y)-c)\,\hat{\psi}_y + \hat{\psi}\, d\bar{U}/dy$, and thus we get

$$-kc(\cosh k + A \sinh k + \sinh k + A \cosh k) + (\cosh k + A \sinh k) = 0,$$
$$-k(1-c)\,(A - \cosh k\bar{W}/\sinh k\bar{W}) - 1 = 0.$$

From these two equations we obtain

$$A = \cosh k\overline{W}/\sinh k\overline{W} - \frac{1}{k(1-c)}, \tag{A 1}$$

$$c^2 - \left(1 - \frac{1-\omega}{1+\omega}\frac{(1-\mathrm{e}^{-2k})}{2k}\right)c + \frac{k\cosh k + k\omega\sinh k - \sinh k}{k^2\,\mathrm{e}^k(1+\omega)} = 0, \tag{A 2}$$

$$\omega = \coth k\overline{W}.$$

As $k \to 0$ with $\overline{W}$ fixed we have $\omega \to 1/k\overline{W}$, and the limit of (A 2) becomes $c^2 - 2c + 1 = 0$, which has the double root $c = 1$. On the other hand as $\overline{W} \to 0$ with k fixed the limit of (A 2) becomes $c^2 - (1+\beta)c + \beta = 0$ where $\beta = (1-\mathrm{e}^{-2k})/2k$, and there are two real roots of this equation. Therefore all finite wavelengths have zero growth rate for sufficiently small $\overline{W}$. The calculated marginal stability relation (table 1) shows that $\overline{W}(k)$ increases from zero as k increases from zero to its cutoff value, but for 'small' $\overline{W}$ the half-wavelength (πk) of the amplifying disturbances is so long that for our purpose (viz. figure 1*a*) we may say that small values of $\overline{W}$ are 'essentially' stable to infinitesimal-amplitude disturbances.

REFERENCES

Blackwelder, R. F. & Kaplan, R. E. 1976 On the wall structure of the turbulent boundary layer. *J. Fluid Mech.* **76**, 89.

Hinze, J. O. 1959 *Turbulence*. McGraw-Hill.

Landahl, M. T. 1975 Wave breakdown and turbulence. *SIAM J. Appl. Math.* **28**, 735.

Lasheras, J. C., Cho, J. S. & Maxworthy, T. 1986 On the origin and evolution of streamwise vortical structures in a plane, free shear layer. *J. Fluid Mech.* **172**, 231.

Orszag, S. A. & Kells, L. C. 1980 Transition to turbulence in plane Poiseuille flow and plane Couette flow. *J. Fluid Mech.* **96**, 159.

Pozrikidis, C. & Higdon, J. J. L. 1985 Nonlinear Kelvin–Helmholtz instability of a finite vortex layer. *J. Fluid Mech.* **157**, 225–263.

Reynolds, W. C. & Tiederman, W. G. 1967 Stability of turbulent channel flow, with application to Malkus's theory. *J. Fluid Mech.* **27**, 253.

Send, U. 1988 Vorticity and instability during flow reversals on the continental shelf. *J. Phys. Oceanogr.* (submitted).

Stern, M. E. 1986 On the amplification of convergences in coastal currents etc. *J. Mar. Res.* **44**, 403.

Stern, M. E. & Pratt, L. J. 1985 Dynamics of vorticity fronts. *J. Fluid Mech.* **161**, 513.

Stern, M. E. & Vorapayev, S. I. 1984 Formation of vorticity fronts in shear flow. *Phys. Fluids* **27**, 848.